iScience

Article

Three-dimensional characteristics of T cells and vasculature in the development of mouse esophageal cancer

Graphical abstract

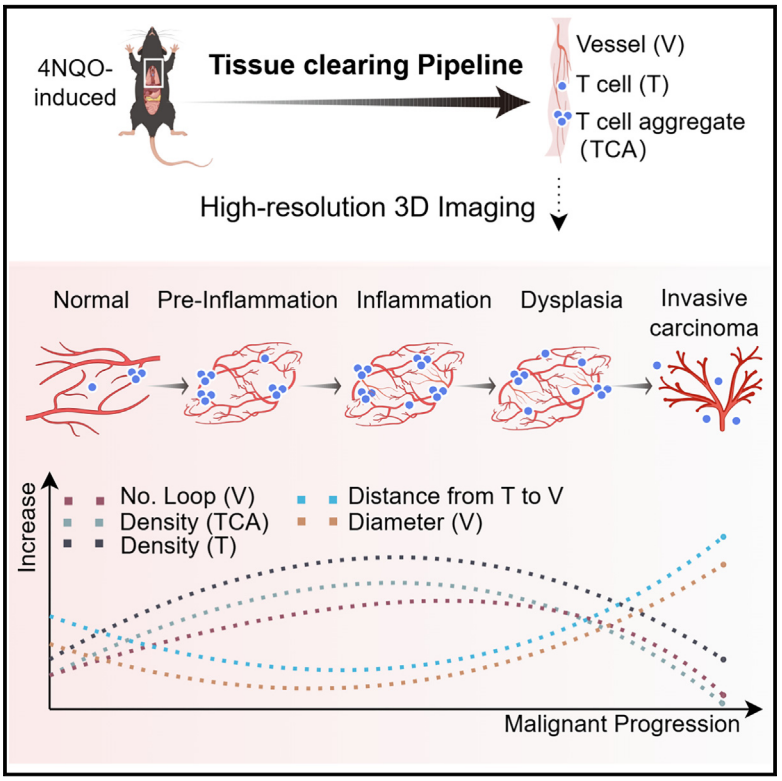

Highlights

- Developed a tissue clearing pipeline for multistage development of mouse ESCC
- High-resolution 3D imaging and quantitative analysis of vessels and T cells
- Spatial proximity of vessels and T cells compared to random distribution model
- Vascular remodeling near T cell aggregates mainly occurred at the inflammatory stage

Authors

Shanshan Bi, Yueguang Wu, Ning Ding, ..., Heyang Cui, Weimin Zhang, Yongping Cui

Correspondence

zhangweimin@bjmu.edu.cn (W.Z.), cuiyp@sphmc.org (Y.C.)

In brief

Vascular remodeling; Immune response; Cancer.

Bi et al., 2024, iScience 27, 111380
December 20, 2024
https://doi.org/10.1016/j.isci.2024.111380

CellPress

iScience

CellPress
OPEN ACCESS

Article

Three-dimensional characteristics of T cells and vasculature in the development of mouse esophageal cancer

Shanshan Bi,[1,2] Yueguang Wu,[1,2] Ning Ding,[1,2] Yan Zhou,[2,3] Huijuan Liu,[2,3] Yongjia Weng,[1,2] Qiqin Song,[1,2] Li Zhang,[1,2] Matthew Yibo Cheng,[1,2] Heyang Cui,[1,2,5] Weimin Zhang,[1,2,3,4,*] and Yongping Cui[1,2,3,4,6,*]

[1]Cancer Institute, Shenzhen Peking University-the Hong Kong University of Science and Technology Medical Center, Shenzhen 518035, P.R. China

[2]Institute of Cancer Research, Shenzhen Bay Laboratory, Shenzhen 518132, P.R. China

[3]Key Laboratory of Cellular Physiology of the Ministry of Education, Department of Pathology, Shanxi Medical University, Taiyuan 030001, P.R. China

[4]State Key Laboratory of Molecular Oncology, Beijing Key Laboratory of Carcinogenesis and Translational Research, Laboratory of Molecular Oncology, Peking University Cancer Hospital & Institute, Research Unit of Molecular Cancer Research, Chinese Academy of Medical Sciences, Beijing 100142, P.R. China

[5]Department of Surgery, Faculty of Medicine, The Chinese University of Hong Kong, Hong Kong, SAR, China

[6]Lead contact

*Correspondence: zhangweimin@bjmu.edu.cn (W.Z.), cuiyp@sphmc.org (Y.C.)

https://doi.org/10.1016/j.isci.2024.111380

SUMMARY

Esophageal squamous cell carcinoma (ESCC) is a common malignancy, characterized by a multistep pathogenic process regulated spatiotemporally within the esophageal epithelial microenvironment, including vessel normalization and immune infiltration. However, empirical evidence elucidating esophageal vascular remodeling and immune infiltration during ESCC tumorigenesis *in situ* is lacking. In this study, utilizing a mouse model recapitulating progressive human ESCC stages, we established a tissue clearing workflow for three-dimensional visualization and analysis of esophageal vessels and T cell distribution. Through this workflow, we delineated the spatial dynamics of vascular remodeling, $CD3^+$ T cells, and characteristic T cell aggregates employing high-resolution light-sheet fluorescence microscopy across five ESCC pathogenic stages. Vessel remodeling might be coupled with T cell infiltration, and their interactions predominantly occurred at the inflammatory stage. These findings provided insights into research methodologies of esophageal cancer and spatiotemporal landscapes of vascular and T cell during ESCC initiation and progression.

INTRODUCTION

Esophageal squamous cell carcinoma (ESCC), the dominant histological subtype of esophageal cancer, is a common digestive malignancy originating from esophageal epithelium.[1] Its poor prognosis is primarily due to the asymptomatic nature of most patients in the early stage, hindering timely diagnosis and treatment.[2] Numerous studies have been dedicated to comprehending ESCC initiation and progression, which typically follows a sequential development paradigm from normal, inflammation, hyperplasia, and dysplasia to carcinoma.[2] The 4-nitroquinoline 1-oxide (4NQO)-induced mouse model faithfully replicates the progressive stages of human ESCC, serving as a valuable tool for investigating tumorigenesis events.[3,4]

In the formation of ESCC, microenvironmental blood vessel plays a critical role to supply nutrients and oxygen to other cellular components.[5–7] Professor Judah Folkman's observations in the 1970s highlighted the heavy vascularization accompanying rapidly growing solid tumors.[8] Although reports of nonangiogenic tumors have emerged recently,[9] neovascularization theory remains relevant to ESCC.[10] In addition, Folkman proposed vascularization blockade as a powerful adjunct for controlling tumor growth.[8] Current antiangiogenic therapies primarily target vessel depletion, vessel normalization, and immune activation.[11] Vessel normalization, known as vascular structural normalization, and immune activation processes appear to be linked, forming a mutually regulatory loop.[12,13] Disrupting vessel normalization may decrease T cell infiltration, while, conversely, T cell depletion or inactivation may hinder vessel normalization.[14]

Growing awareness of vascularity and immunity has raised demand for understanding their spatial heterogeneity.[15] However, traditional spatial studies predominantly rely on tissue sections, limiting 3D characteristics analysis.[16] Advances in tissue clearing have revolutionized this field, enabling easy and effective 3D visualization of whole organs and organisms.[17,18] Tissue clearing includes a range of techniques that make samples transparent for volume imaging. In cancer research, tissue clearing has been applied to certain tumor types, mainly involving morphometric

analysis, vascular 3D observation, and metastatic burden assessment.[19] However, tissue clearing has not been employed in multistage ESCC microenvironment, particularly in relation to the dynamic changes and crosstalk between vasculature and immunity, underscoring the need for methodological refinement.

Here, we integrated a pipeline for 3D imaging and analysis across five stages during ESCC development in a 4NQO-induced mouse model. This pipeline facilitated effective antibody penetration, enabled determination of cleared esophageal histological stages, and provided detailed 3D visualization of the esophageal microenvironment. Utilizing this pipeline, we performed quantitative *in situ* 3D analysis to elucidate the spatiotemporal changes of esophageal mucosal vessels and $CD3^+$ T cells, as well as their potential interactions during ESCC tumorigenesis.

RESULTS

Whole-tissue immunolabeling of multistage esophageal lesions

Various clearing methods, including immunolabeling-enabled DISCO (three-dimensional imaging of solvent-cleared organs) (iDISCO) (Figure 1B),[20] DISCO with superior fluorescence-preserving capability (FDISCO),[21] and clear, unobstructed brain/body imaging cocktails and computational analysis (CUBIC) (Figure S1C),[22] were initially explored for mouse esophagus clearing with promising outcomes. However, preliminary immunolabeling experiments indicated inefficiencies in penetrating esophageal mucosa using these methods, potentially influenced by factors such as tissue properties, choice of antibody, staining time, and procedure. Therefore, we optimized these parameters and ultimately established three immunolabeling approaches that achieved complete antibody penetration in the esophagus (Figure 1C). The passive-wildDISCO method used passive incubation of immunolabeling of wildtype mice and DISCO clearing (wildDISCO) staining solution without a pump. The centrifugation method involved centrifugation and gradient penetration to enhance antibody penetration. The prolonged incubation method significantly extended the recommended iDISCO antibody incubation and washing time. For imaging, light-sheet fluorescence microscopy (LSFM) was selected due to its faster imaging speed and lower phototoxicity compared to confocal microscopy (Figure S1E).[23]

To determine the histological stage of each esophagus, cleared tissue was embedded in paraffin and consecutively sectioned for hematoxylin and eosin (H&E) examination. Consequently, we obtained five stages during ESCC tumorigenesis in 4NQO-exposed mice (Figures 1D and S1A): normal (NOR), preinflammation (PINF), inflammation (INF), dysplasia (DYS), and invasive carcinoma (ICA). Thereafter, we integrated a pipeline for 3D imaging and analysis across multiple pathogenic stages during mouse ESCC development (Figure 1A).

3D visualization of blood vessels during ESCC tumorigenesis

Using this pipeline, we observed esophageal vessels during ESCC tumorigenesis. We examined the imaging depth of LSFM, which showed the mean fluorescence intensity decrease of less than 30% within 1,000 μm working distance, permitting clear distinction of blood vessels (Figure 2A). To preserve staining integrity, vessels were labeled with the endothelial marker CD31 (Video S1). The epithelium stained with DAPI was identified based on its morphological characteristics and signal intensity. Three-dimensional fluorescently stained esophageal vessels were severely tortuous and disorganized during ESCC tumorigenesis (Figure 2B). Additionally, we found that several large vessels originated from the outside of muscularis and extended to the mucosa (Figure 2B, arrows), expanding radially into the tumor (Figure 2C).

Remodeling of mucosal vasculature throughout ESCC tumorigenesis

In a z stack of CD31-stained vessels, three different mucosal or tumor regions of interest (ROIs) were randomly selected for computational modeling, with a per cubic volume of approximately $700 \times 250 \times 40\ \mu m^3$ to $600 \times 300 \times 60\ \mu m^3$ (Figure 3A). Considering the variable position of the esophageal epithelium in each XY plane, a 3D cubic volume representing mucosa comprised not only epithelium but also less adjacent lamina propria (Figure S2A). The vascular computational models were generated automatically and manually to ensure accurate alignment (Video S2).

We investigated vascular remodeling across five stages (Figure S2B). The analyses revealed that vascular remodeling, characterized by reduced vascular volume, length, area, diameter, and increased vascular branches, began as early as PINF and continued during PINF to DYS transition, while, conversely, opposite structural variations were observed in the tumor (Figure 3B). Additionally, vascular perfusion resistance decreased during ESCC tumorigenesis (Figure 3B). Strikingly, there was a significant increase in vascular loop structure and a decrease in straightness (Figures 3C and 3D), indicating the redistribution of blood flow and oxygen. The loop structure, representing vessel connections, as well as vascular tortuosity might contribute to elevated tissue PO_2.[24]

High-resolution imaging and quantitative analysis of T cells and T cell aggregates

The interplay between vessel normalization and T cell infiltration suggests a mutually regulatory loop.[14] To visualize each $CD3^+$ T cell distinctly, a custom 10× objective was employed in LSFM for 3D imaging (Figure 4A), ensuring meticulous assessment of staining specificity to eliminate potential false positives (Figures 4B and S3 and Video S3).

Esophageal infiltrating $CD3^+$ T cells localized either in the mucosa or in the muscularis, with notably lower T cell densities in the latter (Figure 4C). Additionally, $CD3^+$ T cells exhibited aggregation within the mucosa during ESCC tumorigenesis (Figure 4A). Quantitative analysis depicted an initial increase followed by a decline in the density of mucosal $CD3^+$ T cells, reaching peak levels at the stage of INF (Figure 4D). Furthermore, $CD3^+$ T cells were grouped based on their proximity to the tumor margin, revealing higher densities adjacent to the tumor margin that gradually diminished with distance (Figure 4E).

Spatial proximity of T cells and vessels

3D projection and optical section showed that the majority of $CD3^+$ T cells were located in close proximity to vessels (Figure 5A).

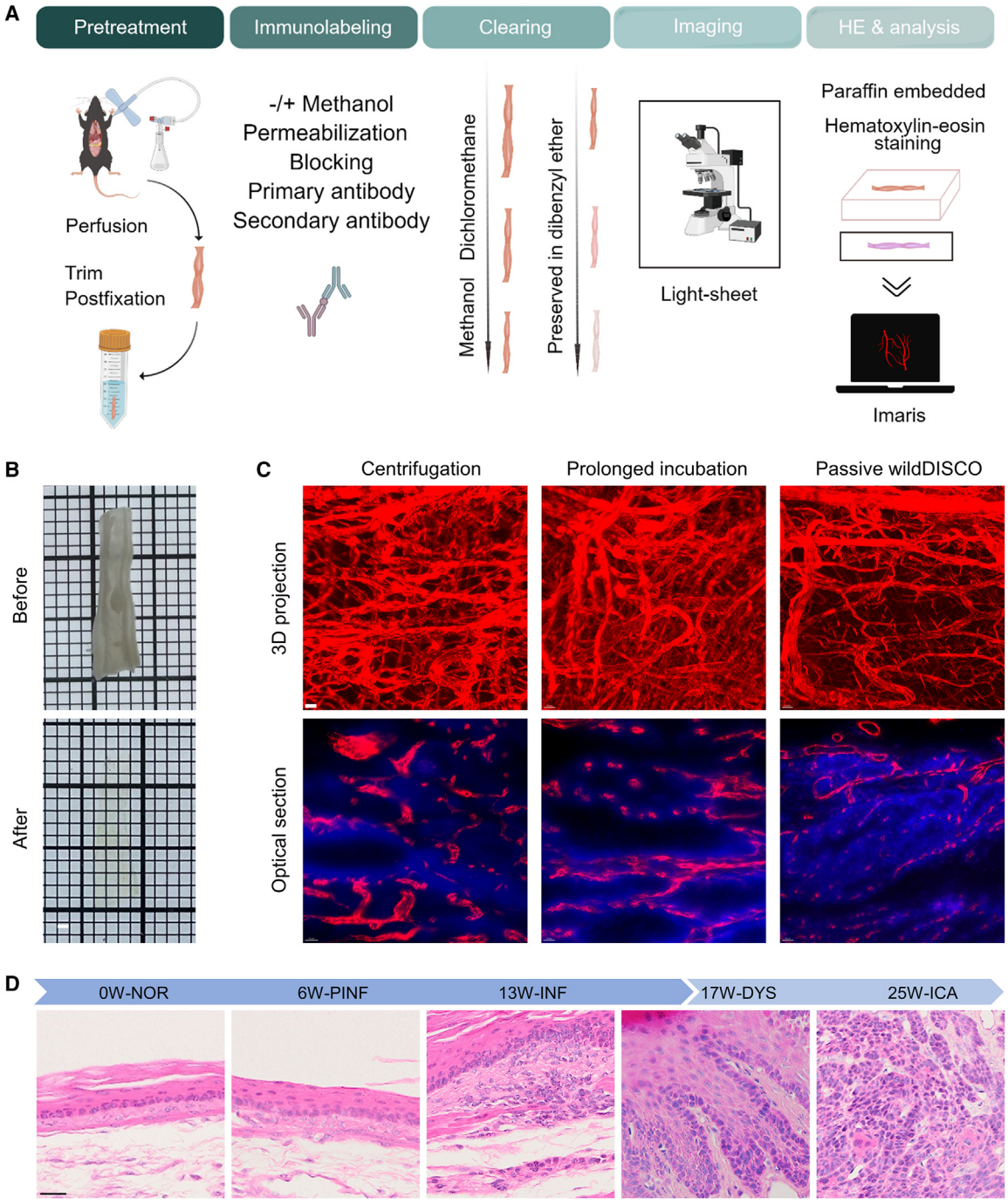

Figure 1. Experimental workflow for tissue clearing of 4NQO-induced multistage esophageal lesions

(A) Experimental outline.

(B) Representative image of mouse esophagus before and after clearing using iDISCO clearing method. Scale bar, 1 mm.

(C) Images demonstrating the three optimized immunolabeling methods. Red: CD31, blue: DAPI. Scale bar, 30 μm.

(D) H&E staining of esophageal tissues identified five different stages: normal (NOR), pre-inflammation (PINF), inflammation (INF), dysplasia (DYS), and invasive carcinoma (ICA). Mice were treated with 4NQO (see also Figure S1A) and sacrificed at week 0, 6, 13, 17, and 25 after treatment. Scale bar, 30 μm.

To quantitatively analyze this association, we measured the shortest distance from vessels to $CD3^+$ T cells or to 3D random spots,[25] which represent a theoretical spatial random distribution model (Figure 5B and Video S4). Compared to random spots, T cells were significantly closer to vessels (Figure 5C). Next, we observed this phenomenon at different pathogenic stages

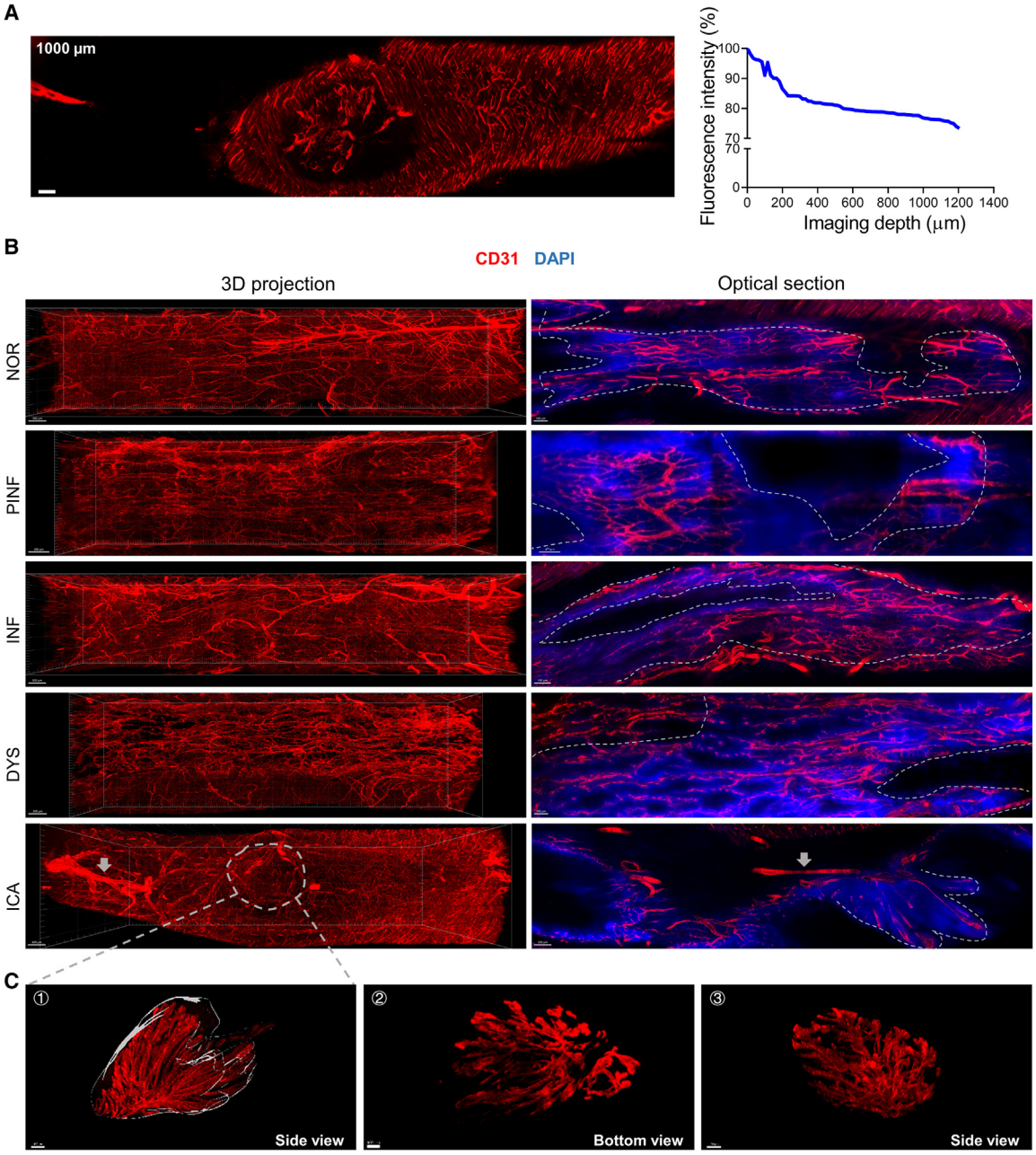

Figure 2. 3D representation of esophageal microvasculature

(A) Optical section displaying esophageal vessels at an imaging depth of 1,000 μm (left). The change in mean fluorescence intensity with imaging depth for LSFM (right, $n = 1$). Scale bar, 200 μm.

(B) 3D visualization (left panel) and optical sections (right panel) of vasculature across five stages during ESCC development ($n = 3$ mice). Scale bars: 300 μm (left panel: NOR to DYS), 100 μm (right panel: NOR to DYS). Scale bar: 400 μm (left: ICA), 200 μm (right: ICA). The white lines demarcated the esophageal mucosa or tumor region, while the presence of black areas in each 2 μm XY plane is due to esophageal curvature. Arrows indicated large vessels originating from the outside of muscularis and extending to the tumor base.

(C) Radiating vessels in the tumor. Scale bars, 100 μm.

(Figure S4). T cells were found near vessels at the PINF (12.74 μm), INF (12.54 μm), and DYS (13.5 μm) stages in comparison to the NOR stage (14.4 μm, Figure 5D), while the distance between T cells and vessels relatively increased at the DYS stage compared to PINF and INF stages (Figure 5D), possibly due to decreased T cell infiltration. When T cell locations were categorized at 4 μm intervals, dynamic changes further confirmed the relationship between T cell infiltration and vessels during ESCC

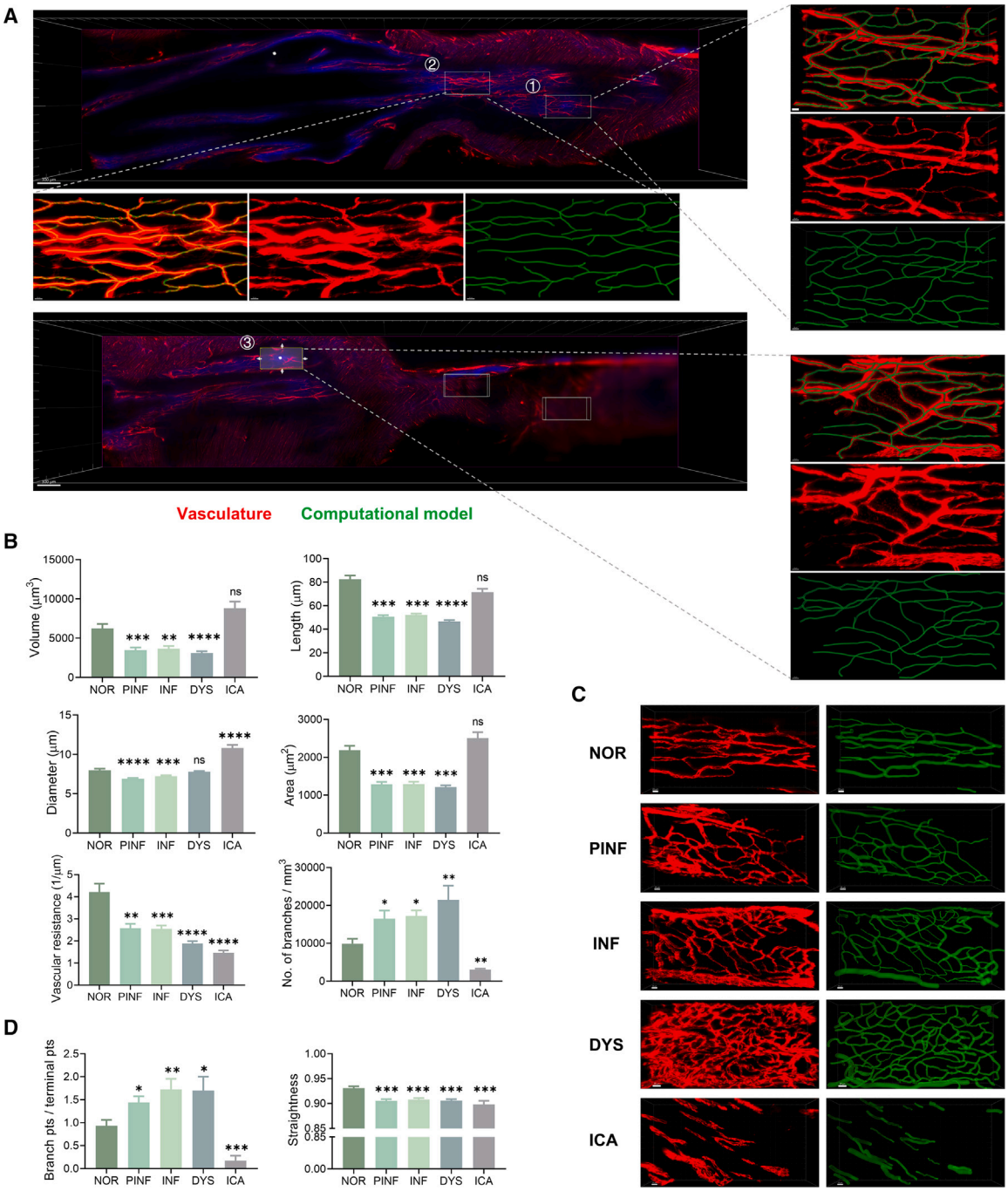

Figure 3. Computational reconstruction and analysis of esophageal mucosal vasculature

(A) Three regions in each esophagus were selected for quantification (n = 3 mice per group). The upper and lower sectional images represented two different XY planes of a normal esophageal tissue stained with CD31 (red) and DAPI (blue). Scale bars: 20 μm (selected regions), 300 μm (entire esophagus). See also Figure S2B.

(B) Quantification of vessel volume, vessel length, vessel area, vessel diameter, vascular branch, and vessel perfusion resistance (the formula is explained in Imaris) in a total of nine regions across each stage.

(C) 3D images of CD31$^+$ vasculature and computational model displaying changes in loop structure. Scale bars, 20 μm.

(D) Quantification of vessel branch points versus terminal points, indicating the relative level of loop structure, and vessel straightness. Unpaired t tests or Mann-Whitney U tests. All data represented mean ± SEM. *p < 0.05, **p < 0.01, ***p < 0.001, ****p < 0.0001.

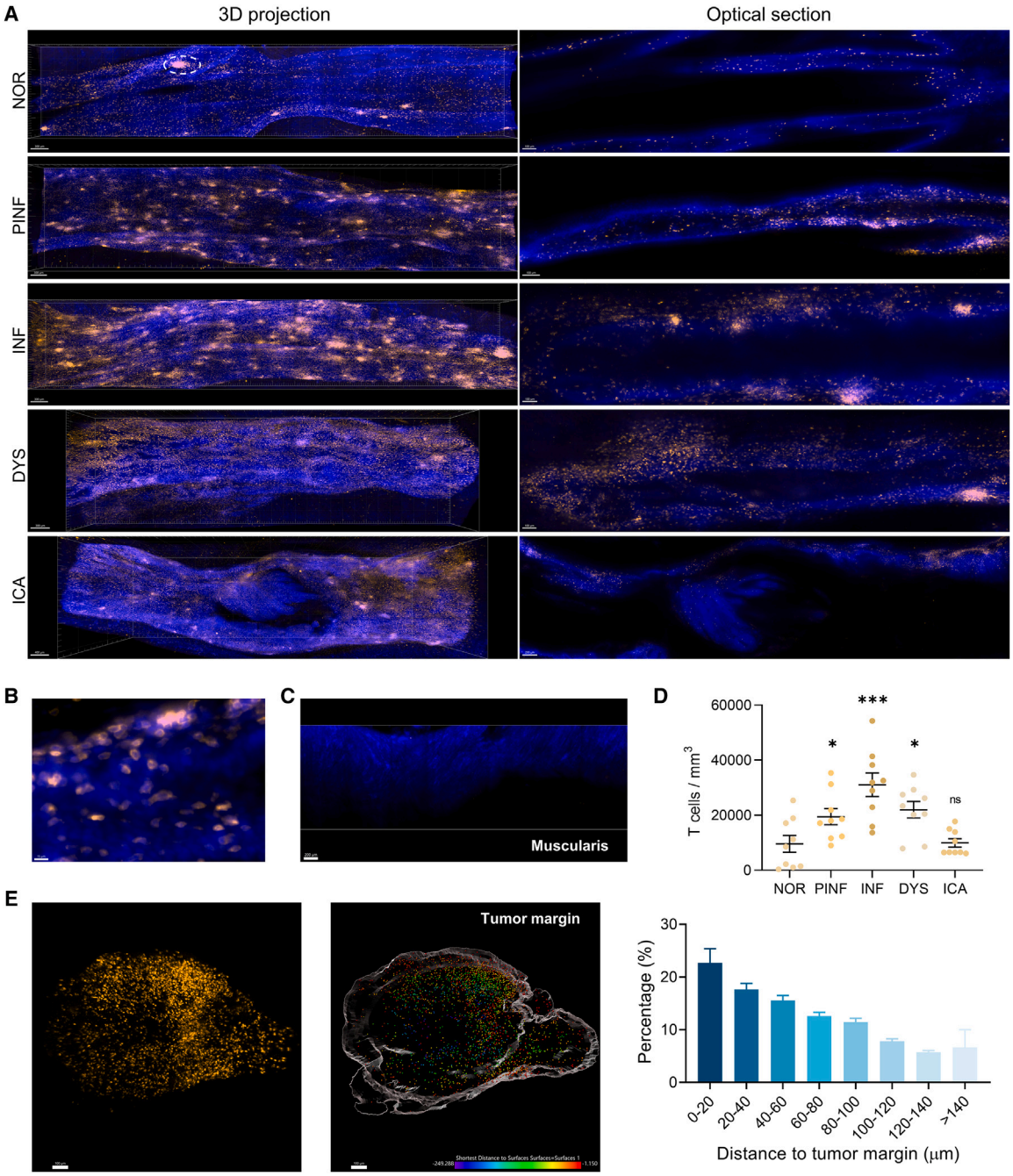

Figure 4. 3D representation and quantification of esophageal T cells

(A) 3D images (left panel) and optical sections (right panel) of esophageal CD3$^+$ T cells (yellow) (n = 3 mice per stage). The white line demarcated a T cell aggregate. Scale bars: 300 μm (left panel: NOR to DYS), 100 μm (right panel: NOR to DYS). Scale bar: 400 μm (left: ICA), 200 μm (right: ICA).

(B) Zoomed-in LSFM image showing esophageal mucosal T cells. Scale bar, 15 μm.

(C) Optical section of the esophageal muscularis depicting low T cell density. Scale bar, 200 μm.

(D) Quantification of T cells per mm^3 mucosal volume. Each dot represented a region equivalent to the volume analyzed for vessels mentioned above. Unpaired t tests or Mann-Whitney U test. All data represented mean ± SEM. *p < 0.05, ***p < 0.001.

(E) 3D images (left) and rendering (middle) of T cells in the tumor. Scale bars, 100 μm. The percentage of CD3$^+$ T cells within a defined distance to the tumor margin (n = 3 tumors) (right).

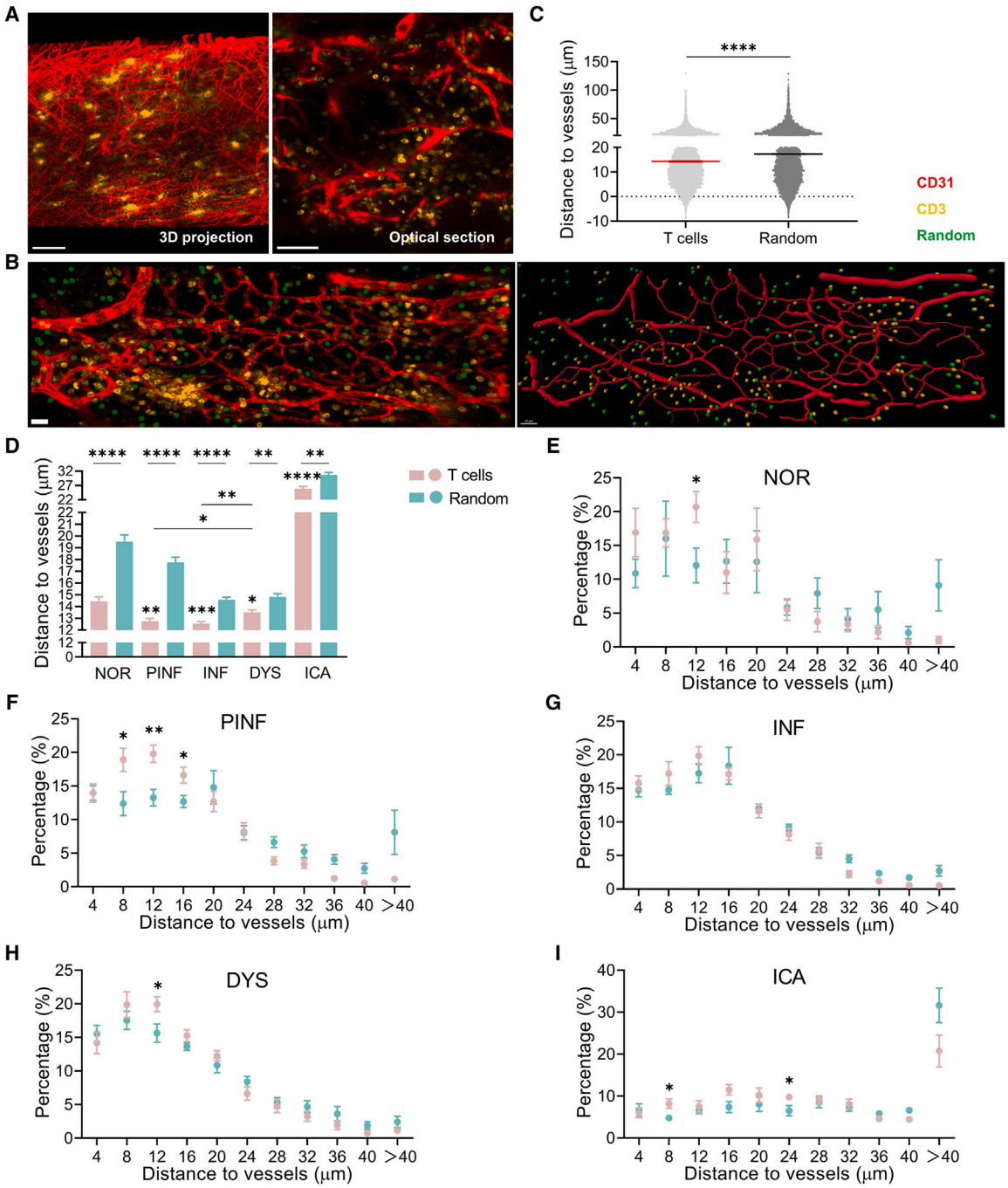

Figure 5. T cells localize near vessels

(A) Images of CD3$^+$ T cells (yellow) and CD31$^+$ vessels (red). Scale bar: 300 μm (left), 50 μm (right). See also Figure S4.

(B) 3D visualization (left) and computational reconstruction (right) of mucosal vasculature and T cells. Random spots (green) represent a theoretical spatial random distribution model. Scale bars, 30 μm.

(C) Distance to the nearest vessel for 7,150 T cells or random spots from 15 mice was analyzed.

(D) Shortest distance from T cells or random spots to the nearest vessels in 9 regions per stage.

(E–I) T cell distribution around the vessels across five stages. A total of (E) 820, (F) 1,418, (G) 2,462, (H) 1,788, and (I) 662 T cells or random spots were analyzed in 3 mice. Unpaired t tests or Mann-Whitney U tests. All data represented mean ± SEM. *$p < 0.05$, **$p < 0.01$, ***$p < 0.001$, ****$p < 0.0001$.

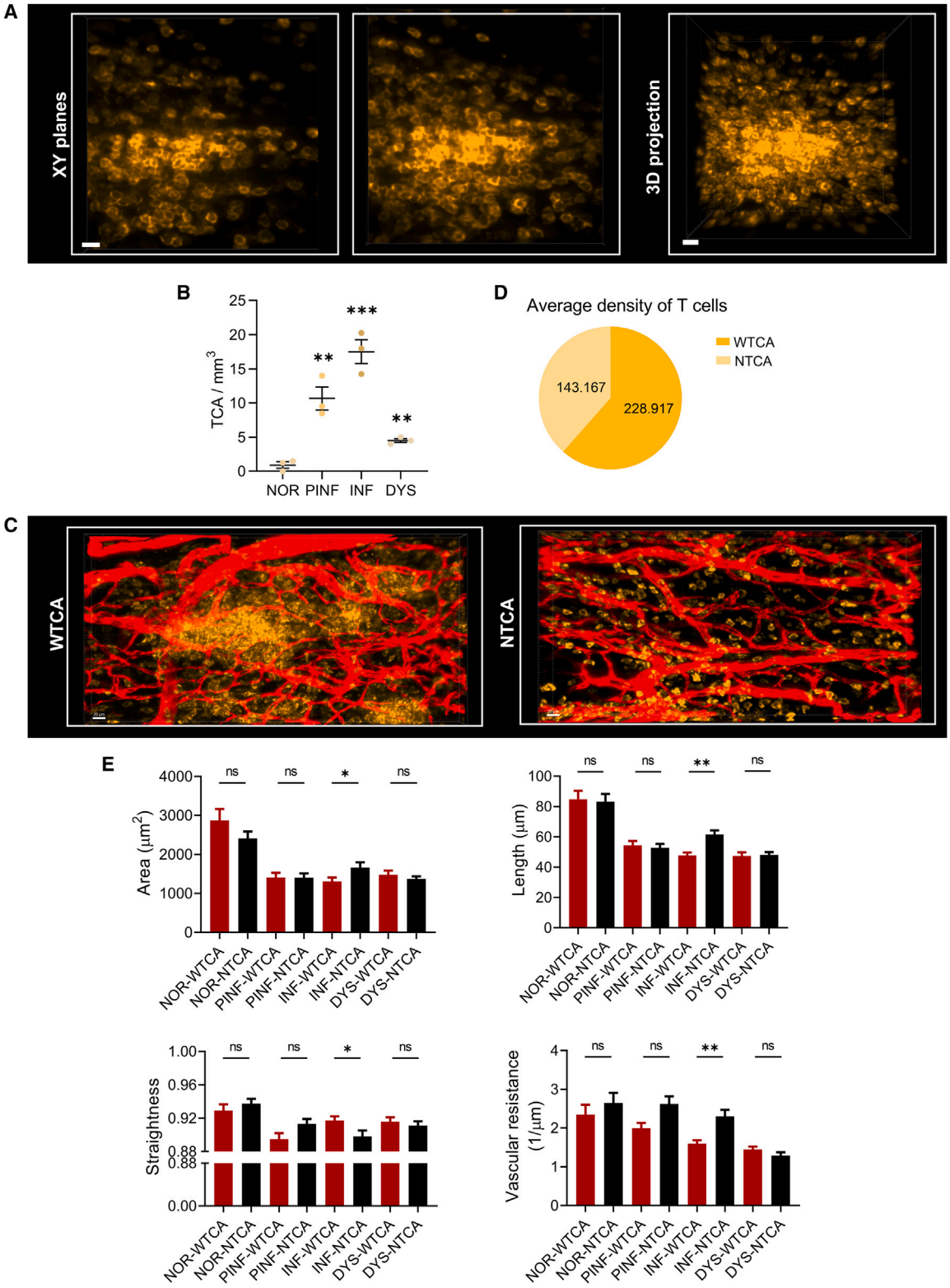

Figure 6. T cell aggregates induce local vascular remodeling during inflammation

(A) Different XY planes and 3D projection of $CD3^+$ T cell aggregates (TCAs). Scale bars, 15 μm.

(B) Quantification of the TCA per mm^3 esophageal volume. Each dot represented an esophagus.

(legend continued on next page)

tumorigenesis. Specifically, T cells were predominantly located within 8–12 μm of vessels under physiological conditions (Figure 5E). During the NOR to PINF transition, T cells gradually infiltrated and became enriched within 4–16 μm of vessels (Figure 5F). In the INF stage, T cells might have already formed functional niches randomly located around vessels (Figure 5G). After INF, they gradually decreased and eventually returned to their initial location within 8–12 μm of vessels (Figure 5H). Additionally, $CD3^+$ T cells within the tumor were mainly trafficked to 4–8 and 20–24 μm of vessels (Figure 5I and Video S5), indicating potential T cell infiltration and a specific immune zone around tumor vasculature.

T cell aggregates drive local vascular remodeling predominantly at the inflammatory stage

Next, we examined the spatial interactions between T cells and blood vessels. Considering that vascular network is composed of multiple vascular segments, bias might be introduced if we analyzed several segments adjacent to T cells (Figure S5A). We then noted the presence of characteristic T cell aggregates (TCAs) comprising substantial $CD3^+$ T cells (Figure 6A), which might be tertiary lymphoid structures (TLSs) with potential functional interplay with vessels (Figure S6).[26–28] Dynamic changes in TCA were consistent with those in mucosal T cells, while TCA eventually disappeared in the tumor core (Figure 6B).

Here, we computed vascular remodeling in the regions with TCA (WTCA), setting an equivalent region of vessels without the TCA as the control (NTCA, Figure 6C). The density of T cells was higher in WTCA compared to NTCA (Figure 6D). Our analysis indicated that vascular remodeling near TCA, including decreased vascular length, area, resistance, and increased straightness, mainly occurred at the INF stage (Figures 6E and S5B). These results strongly suggested that stage INF represents a crucial turning point for the fate of blood vessels and T cells during ESCC tumorigenesis.

DISCUSSION

In this study, we developed an effective pipeline for three-dimensional analysis of mouse esophageal tissues at various pathogenic stages of ESCC, providing insights into the microenvironmental landscape. Utilizing optimized immunolabeling methods, we observed vascular remodeling, depicted dynamic spatial mapping of T cells, and identified characteristic TCAs. Vessel normalization is considered as a response to antiangiogenic therapy[29] and improves survival when combined with immune activation.[30] Our 3D analysis confirmed that T cells resided near vascular niches during ESCC tumorigenesis and strong crosstalk between vessel normalization and host T cells predominantly occurred at the inflammatory stage.

Given the challenges of obtaining continuous multistage esophageal lesions from human individual, we used a mouse model that imitates human ESCC development and offers valuable insights into the tumor microenvironment and gene expression dynamics.[4]

Tissue clearing has enabled 3D labeling and imaging of mouse body and parts of human organs. Previous passive labeling methods, such as iDISCO, CUBIC, and FDISCO, mainly rely on transgenically expressed proteins or small-molecule dyes, while immunoglobulin G (IgG) antibodies often struggle to consistently penetrate various esophageal tissue layers within the recommended methods. Active labeling methods using electric field or cardiac pumps, such as clear lipid-exchanged acrylamide-hybridized rigid imaging/immunostaining/in situ hybridization-compatible tissue-hydrogel (CLARITY)[31] and wildDISCO,[32] while effective, can be costly, complex, or disruptive for individual tissue. Furthermore, precise histological categories of cleared esophageal lesions have not been reported, although we found that the diagnosing immunolabelled paraffin-embedded cleared organs (DIPCO)[33] method that involves tissue re-embedding may offer utility in this regard. Moreover, employing a custom LSFM objective, we obtained 3D images with subcellular resolution to ensure staining specificity across mouse esophageal multistage lesions.

Although previous studies have demonstrated increased vascular density in the early stages of ESCC on histological sections,[6,34] when and how ESCC vascular remodeling takes place are largely unknown. Our results showed that vascular remodeling began as early as pre-inflammation, characterized by decreased vessel diameter, volume, area, and length and increased vessel branches before the ICA stage, while, conversely, opposite structural variations were observed in the radiating ESCC vasculature. Another interesting finding was the increased vascular loops before ESCC formation, likely due to the inflammation-induced angiogenic sprouting,[35] potentially indicative of improved tissue oxygen tension,[24] while tortuosity and decreased loop structure in the tumor vasculature indicated significant vascular alterations and a relatively hypoxic microenvironment niche that might attract and sequester immune cells in the tumor.[36] Tumor vasculature is typically dilated, indicating increased diameter,[37] and tortuous. Tortuous vessels are common angiographic findings,[38] and the tortuosity index has been used to assess diseases in clinical screenings.[39] Additionally, although tumor microvascular density was increased in previous histological examination, our results suggested a reduction in vascular branch at the 3D level, which was related to decreased vascular connections (loops) in the radiating vessels, as the calculation of vascular branches was based on the number of vascular segments divided by the region volume. Similarly to the folded, expanded, and tortuous vessels reported in some tumors, the folded layer-like vessels in ESCC might also lead to variations and deviation in two-dimensional examination.[40] Currently, the dynamic changes in vasculature before tumor formation remain largely unknown, due partly to the scarcity of animal models that can effectively mimic tumor progression and partly to the difficulty in clinically mapping microvascular formation.[41] Future studies should focus on

(C) WTCA: regions of TCA and adjacent vessels. NTCA: equivalent regions of vessels without TCA. Scale bars, 20 μm.
(D) Average density of $CD3^+$ T cells in 12 ROIs of WTCA or NTCA.
(E) Quantification of vessel straightness, vessel perfusion resistance, vessel area, and vessel length in 3 WTCA or NTCA per stage. Two-tailed unpaired t tests. All data represented mean ± SEM. $^*p < 0.05$, $^{**}p < 0.01$, $^{***}p < 0.001$. See also Figure S5B.

angiogenesis by employing *ex vivo* 3D imaging techniques or developing advanced devices and toolkits for high-resolution *in vivo* imaging, with the potential to enable early screening through the detection of vascular morphology.

Our quantitative *in situ* 3D analysis unveiled dynamic distribution of T cells and TCAs during ESCC tumorigenesis. It is demonstrated that T cells rely on functional vasculature to enter tissue[42] and there are mutual interactions between T cells and blood vessels.[14,43] We found that T cells specifically resided near blood vessels, with distances potentially correlating with T cell infiltration dynamics, shortest at the inflammatory stage. Interestingly, T cells were preferentially located within 8–12 μm of vessels under physiological condition (NOR) and potential functional exhaustion period (DYS), while the INF stage was observed to contain randomly distributed T cells. Furthermore, T cells were enriched within 4–8 μm of vessels at the stage of PINF and ICA, which is likely associated with immune infiltration area. Strikingly, the phenotypes of TCA in this study were similar to TLSs, which are characterized by a region of B cells surrounded by $CD3^+$ T cells and are found in cancer-induced chronic inflammation.[28] Although the specific cellular composition in different tumor TLSs varies, $CD4^+$ T cells usually predominate in T cell zones, further indicating that TCA might be TLS (Figure S6). TLSs are intimately linked to the recruitment of immune cells, improved prognosis in immunotherapy, and the secretion of vascular cell adhesion molecule 1.[28,44] Our results of phenotypic characteristics from TCA-driven vascular remodeling suggested potentially heightened immune responses to abnormal vasculature prominently at the inflammatory stage, implicating the crucial role of chronic inflammation in ESCC vascularization.

The clinical development of combined intervention using anti-angiogenic therapy and immunotherapies, possibly through anti-angiogenesis leading to vessel normalization, which counteracts immunosuppressive,[45] was used to successfully treat advanced ESCC.[46] Our results have potential implications for understanding and assessing vascular remodeling and T cell infiltration in ESCC prevention and treatment. We anticipate that 3D imaging methods will find increasing utility in clinical research, addressing limitations inherent in 2D histological methods.

Limitations of the study

Although the parallels in tumor biology between the mouse model and human ESCC provide a valuable foundation,[4,47] the results utilizing 4NQO-induced mouse model should be interpreted with caution when translating to human. Further human validation requires advanced devices for developing *in vivo* high-resolution depth imaging or multistage human esophageal samples for the methodological refinement of tissue clearing, which could simulate our pipeline and spatiotemporal analysis. Furthermore, the applicability and species specificity of commercially available antibodies limited multiplexed labeling, preventing the assessment of the dynamic behavioral characteristics of specific T cells. Therefore, it is necessary to validate suitable antibodies[19,32] for our pipeline or develop other whole-tissue immunolabeling methods, such as multiple rounds of relabeling.[48] Currently, robust data analysis and sharing platforms for tissue clearing are still challenges.

RESOURCE AVAILABILITY

Lead contact

Further information and requests for resources and reagents should be directed to and will be fulfilled by the lead contact, Yongping Cui, cuiyp@sphmc.org.

Materials availability

This study did not generate new unique reagents.

Data and code availability

- Raw data have been deposited at Mendeley Data and are publicly available as of the date of publication at https://doi.org/10.17632/rggyy48rg6.1. Whole-tissue images can be provided by the lead contact upon request.
- This paper does not report original code.
- Any additional information required to reanalyze the data reported in this paper is available from the lead contact upon request.

ACKNOWLEDGMENTS

This work was funded by Guangdong Basic and Applied Basic Research Foundation (2019B030302012), the National Key R&D Program of China (2021YFC2501001 and 2022YFC3401002), Shenzhen Medical Research Fund (C2303002), the Major Program of Shenzhen Bay Laboratory (S201101004), the National Natural Science Foundation of China (82341024, U21A20372, 82172930, 82302916, and 82103143), and Shenzhen "San-Ming" Project of Medicine (SZSM202311014). We thank the Bioimaging Core of Shenzhen Bay Laboratory, Shenzhen PKU-HKUST Medical Center, and Litone Company for providing imaging support and Shenzhen PKU-HKUST Medical Center animal laboratory center staff Xiaodi Chen for animal husbandry.

AUTHOR CONTRIBUTIONS

Conceptualization: Y.C. and W.Z.; methodology: S.B., Y. Wu, N.D., and M.Y.C.; software: S.B., Q.S., and H.C.; formal analysis: S.B., Y.Wu, and N.D.; investigation: Y.C., W.Z., S.B., Y. Wu, N.D., Y.Z., H.L., Y. Weng, and L.Z.; resources: S.B., Y. Wu, N.D., Y. Weng, W.Z., and Y.C.; data curation: S.B., Y.Z., and H.L.; writing – original draft: S.B.; writing – review and editing: Y.C. and W.Z.; supervision: Y.C. and W.Z.; project administration: S.B., Y. Wu, and N.D.; funding acquisition: Y.C., W.Z., N.D., and H.C.

DECLARATION OF INTERESTS

The authors declare no competing interests.

STAR★METHODS

Detailed methods are provided in the online version of this paper and include the following:

- KEY RESOURCES TABLE
- EXPERIMENTAL MODEL AND STUDY PARTICIPANT DETAILS
  - Mice
- METHOD DETAILS
  - Sample collection and preparation
  - Antibody validation
  - Whole-tissue immunolabeling
  - Esophageal clearing
  - Light-sheet microscopy
  - Histological categories
  - Image processing and analysis
- QUANTIFICATION AND STATISTICAL ANALYSIS

SUPPLEMENTAL INFORMATION

Supplemental information can be found online at https://doi.org/10.1016/j.isci.2024.111380.

Received: May 12, 2024
Revised: September 26, 2024
Accepted: November 11, 2024
Published: November 14, 2024

REFERENCES

1. Morgan, E., Soerjomataram, I., Rumgay, H., Coleman, H.G., Thrift, A.P., Vignat, J., Laversanne, M., Ferlay, J., and Arnold, M. (2022). The Global Landscape of Esophageal Squamous Cell Carcinoma and Esophageal Adenocarcinoma Incidence and Mortality in 2020 and Projections to 2040: New Estimates From GLOBOCAN 2020. Gastroenterology *163*, 649. https://doi.org/10.1053/j.gastro.2022.05.054.

2. Wang, G.Q., Abnet, C.C., Shen, Q., Lewin, K.J., Sun, X.D., Roth, M.J., Qiao, Y.L., Mark, S.D., Dong, Z.W., Taylor, P.R., and Dawsey, S.M. (2005). Histological precursors of oesophageal squamous cell carcinoma: results from a 13 year prospective follow up study in a high risk population. Gut *54*, 187–192. https://doi.org/10.1136/gut.2004.046631.

3. Tang, X.H., Knudsen, B., Bemis, D., Tickoo, S., and Gudas, L.J. (2004). Oral cavity and esophageal carcinogenesis modeled in carcinogen-treated mice. Clin. Cancer Res. *10*, 301–313. https://doi.org/10.1158/1078-0432.ccr-0999-3.

4. Yao, J., Cui, Q., Fan, W., Ma, Y., Chen, Y., Liu, T., Zhang, X., Xi, Y., Wang, C., Peng, L., et al. (2020). Single-cell transcriptomic analysis in a mouse model deciphers cell transition states in the multistep development of esophageal cancer. Nat. Commun. *11*, 3715. https://doi.org/10.1038/s41467-020-17492-y.

5. Bejarano, L., Jordão, M.J.C., and Joyce, J.A. (2021). Therapeutic Targeting of the Tumor Microenvironment. Cancer Discov. *11*, 933–959. https://doi.org/10.1158/2159-8290.Cd-20-1808.

6. Takahashi, K., Asano, N., Imatani, A., Kondo, Y., Saito, M., Takeuchi, A., Jin, X., Saito, M., Hatta, W., Asanuma, K., et al. (2020). Sox2 induces tumorigenesis and angiogenesis of early-stage esophageal squamous cell carcinoma through secretion of Suprabasin. Carcinogenesis *41*, 1543–1552. https://doi.org/10.1093/carcin/bgaa014.

7. Herbert, S.P., and Stainier, D.Y.R. (2011). Molecular control of endothelial cell behaviour during blood vessel morphogenesis. Nat. Rev. Mol. Cell Biol. *12*, 551–564. https://doi.org/10.1038/nrm3176.

8. Folkman, J. (1971). Tumor angiogenesis: therapeutic implications. N. Engl. J. Med. *285*, 1182–1186. https://doi.org/10.1056/nejm197111182852108.

9. Donnem, T., Reynolds, A.R., Kuczynski, E.A., Gatter, K., Vermeulen, P.B., Kerbel, R.S., Harris, A.L., and Pezzella, F. (2018). Non-angiogenic tumours and their influence on cancer biology. Nat. Rev. Cancer *18*, 323–336. https://doi.org/10.1038/nrc.2018.14.

10. Guo, X., Meng, X., and Liu, R. (2021). Prognostic value of microvessel density in esophageal squamous cell carcinoma-a systematic review and meta-analysis. Pathol. Res. Pract. *227*, 153644. https://doi.org/10.1016/j.prp.2021.153644.

11. Lugano, R., Ramachandran, M., and Dimberg, A. (2020). Tumor angiogenesis: causes, consequences, challenges and opportunities. Cell. Mol. Life Sci. *77*, 1745–1770. https://doi.org/10.1007/s00018-019-03351-7.

12. Huang, Y., Yuan, J., Righi, E., Kamoun, W.S., Ancukiewicz, M., Nezivar, J., Santosuosso, M., Martin, J.D., Martin, M.R., Vianello, F., et al. (2012). Vascular normalizing doses of antiangiogenic treatment reprogram the immunosuppressive tumor microenvironment and enhance immunotherapy. Proc. Natl. Acad. Sci. USA *109*, 17561–17566. https://doi.org/10.1073/pnas.1215397109.

13. Tian, L., Goldstein, A., Wang, H., Ching Lo, H., Sun Kim, I., Welte, T., Sheng, K., Dobrolecki, L.E., Zhang, X., Putluri, N., et al. (2017). Mutual regulation of tumour vessel normalization and immunostimulatory reprogramming. Nature *544*, 250–254. https://doi.org/10.1038/nature21724.

14. Huang, Y., Kim, B.Y.S., Chan, C.K., Hahn, S.M., Weissman, I.L., and Jiang, W. (2018). Improving immune-vascular crosstalk for cancer immunotherapy. Nat. Rev. Immunol. *18*, 195–203. https://doi.org/10.1038/nri.2017.145.

15. Takahashi, K., Abe, K., Kubota, S.I., Fukatsu, N., Morishita, Y., Yoshimatsu, Y., Hirakawa, S., Kubota, Y., Watabe, T., Ehata, S., et al. (2022). An analysis modality for vascular structures combining tissue-clearing technology and topological data analysis. Nat. Commun. *13*, 5239. https://doi.org/10.1038/s41467-022-32848-2.

16. Liu, X., Zhao, S., Wang, K., Zhou, L., Jiang, M., Gao, Y., Yang, R., Yan, S., Zhang, W., Lu, B., et al. (2023). Spatial transcriptomics analysis of esophageal squamous precancerous lesions and their progression to esophageal cancer. Nat. Commun. *14*, 4779. https://doi.org/10.1038/s41467-023-40343-5.

17. Ueda, H.R., Ertürk, A., Chung, K., Gradinaru, V., Chédotal, A., Tomancak, P., and Keller, P.J. (2020). Tissue clearing and its applications in neuroscience. Nat. Rev. Neurosci. *21*, 61–79. https://doi.org/10.1038/s41583-019-0250-1.

18. Richardson, D.S., and Lichtman, J.W. (2015). Clarifying Tissue Clearing. Cell *162*, 246–257. https://doi.org/10.1016/j.cell.2015.06.067.

19. Almagro, J., Messal, H.A., Zaw Thin, M., van Rheenen, J., and Behrens, A. (2021). Tissue clearing to examine tumour complexity in three dimensions. Nat. Rev. Cancer *21*, 718–730. https://doi.org/10.1038/s41568-021-00382-w.

20. Renier, N., Wu, Z., Simon, D.J., Yang, J., Ariel, P., and Tessier-Lavigne, M. (2014). iDISCO: a simple, rapid method to immunolabel large tissue samples for volume imaging. Cell *159*, 896–910. https://doi.org/10.1016/j.cell.2014.10.010.

21. Qi, Y., Yu, T., Xu, J., Wan, P., Ma, Y., Zhu, J., Li, Y., Gong, H., Luo, Q., and Zhu, D. (2019). FDISCO: Advanced solvent-based clearing method for imaging whole organs. Sci. Adv. *5*, eaau8355. https://doi.org/10.1126/sciadv.aau8355.

22. Susaki, E.A., Tainaka, K., Perrin, D., Kishino, F., Tawara, T., Watanabe, T.M., Yokoyama, C., Onoe, H., Eguchi, M., Yamaguchi, S., et al. (2014). Whole-brain imaging with single-cell resolution using chemical cocktails and computational analysis. Cell *157*, 726–739. https://doi.org/10.1016/j.cell.2014.03.042.

23. Stelzer, E.H.K., Strobl, F., Chang, B.-J., Preusser, F., Preibisch, S., McDole, K., and Fiolka, R. (2021). Light sheet fluorescence microscopy. Nat. Rev. Methods Primers *1*, 73. https://doi.org/10.1038/s43586-021-00069-4.

24. Goldman, D., and Popel, A.S. (2000). A computational study of the effect of capillary network anastomoses and tortuosity on oxygen transport. J. Theor. Biol. *206*, 181–194. https://doi.org/10.1006/jtbi.2000.2113.

25. Hawkins, E.D., Duarte, D., Akinduro, O., Khorshed, R.A., Passaro, D., Nowicka, M., Straszkowski, L., Scott, M.K., Rothery, S., Ruivo, N., et al. (2016). T-cell acute leukaemia exhibits dynamic interactions with bone marrow microenvironments. Nature *538*, 518–522. https://doi.org/10.1038/nature19801.

26. Sautès-Fridman, C., Petitprez, F., Calderaro, J., and Fridman, W.H. (2019). Tertiary lymphoid structures in the era of cancer immunotherapy. Nat. Rev. Cancer *19*, 307–325. https://doi.org/10.1038/s41568-019-0144-6.

27. Johansson-Percival, A., He, B., Li, Z.J., Kjellén, A., Russell, K., Li, J., Larma, I., and Ganss, R. (2017). De novo induction of intratumoral lymphoid structures and vessel normalization enhances immunotherapy in resistant tumors. Nat. Immunol. *18*, 1207–1217. https://doi.org/10.1038/ni.3836.

28. Schumacher, T.N., and Thommen, D.S. (2022). Tertiary lymphoid structures in cancer. Science *375*, eabf9419. https://doi.org/10.1126/science.abf9419.

29. Jain, R.K. (2001). Normalizing tumor vasculature with anti-angiogenic therapy: a new paradigm for combination therapy. Nat. Med. *7*, 987–989. https://doi.org/10.1038/nm0901-987.

30. Shrimali, R.K., Yu, Z., Theoret, M.R., Chinnasamy, D., Restifo, N.P., and Rosenberg, S.A. (2010). Antiangiogenic agents can increase lymphocyte

infiltration into tumor and enhance the effectiveness of adoptive immunotherapy of cancer. Cancer Res. *70*, 6171–6180. https://doi.org/10.1158/0008-5472.Can-10-0153.

31. Chung, K., Wallace, J., Kim, S.Y., Kalyanasundaram, S., Andalman, A.S., Davidson, T.J., Mirzabekov, J.J., Zalocusky, K.A., Mattis, J., Denisin, A.K., et al. (2013). Structural and molecular interrogation of intact biological systems. Nature *497*, 332–337. https://doi.org/10.1038/nature12107.
32. Mai, H., Luo, J., Hoeher, L., Al-Maskari, R., Horvath, I., Chen, Y., Kofler, F., Piraud, M., Paetzold, J.C., Modamio, J., et al. (2024). Whole-body cellular mapping in mouse using standard IgG antibodies. Nat. Biotechnol. *42*, 617–627. https://doi.org/10.1038/s41587-023-01846-0.
33. Tanaka, N., Kanatani, S., Tomer, R., Sahlgren, C., Kronqvist, P., Kaczynska, D., Louhivuori, L., Kis, L., Lindh, C., Mitura, P., et al. (2017). Whole-tissue biopsy phenotyping of three-dimensional tumours reveals patterns of cancer heterogeneity. Nat. Biomed. Eng. *1*, 796–806. https://doi.org/10.1038/s41551-017-0139-0.
34. Hlatky, L., Hahnfeldt, P., and Folkman, J. (2002). Clinical application of antiangiogenic therapy: microvessel density, what it does and doesn't tell us. J. Natl. Cancer Inst. *94*, 883–893. https://doi.org/10.1093/jnci/94.12.883.
35. De Palma, M., and Hanahan, D. (2024). Milestones in tumor vascularization and its therapeutic targeting. Nat. Can. (Ott.) *5*, 827–843. https://doi.org/10.1038/s43018-024-00780-7.
36. Sattiraju, A., Kang, S., Giotti, B., Chen, Z., Marallano, V.J., Brusco, C., Ramakrishnan, A., Shen, L., Tsankov, A.M., Hambardzumyan, D., et al. (2023). Hypoxic niches attract and sequester tumor-associated macrophages and cytotoxic T cells and reprogram them for immunosuppression. Immunity *56*, 1825–1843.e6. https://doi.org/10.1016/j.immuni.2023.06.017.
37. Jain, R.K. (2005). Normalization of tumor vasculature: an emerging concept in antiangiogenic therapy. Science *307*, 58–62. https://doi.org/10.1126/science.1104819.
38. Han, H.C. (2012). Twisted blood vessels: symptoms, etiology and biomechanical mechanisms. J. Vasc. Res. *49*, 185–197. https://doi.org/10.1159/000335123.
39. Wolf, Y.G., Tillich, M., Lee, W.A., Rubin, G.D., Fogarty, T.J., and Zarins, C.K. (2001). Impact of aortoiliac tortuosity on endovascular repair of abdominal aortic aneurysms: evaluation of 3D computer-based assessment. J. Vasc. Surg. *34*, 594–599. https://doi.org/10.1067/mva.2001.118586.
40. Liu, Y.A., Pan, S.T., Hou, Y.C., Shen, M.Y., Peng, S.J., Tang, S.C., and Chung, Y.C. (2013). 3-D visualization and quantitation of microvessels in transparent human colorectal carcinoma [corrected]. PLoS ONE *8*, e81857. https://doi.org/10.1371/journal.pone.0081857.
41. Breckwoldt, M.O., Bode, J., Kurz, F.T., Hoffmann, A., Ochs, K., Ott, M., Deumelandt, K., Krüwel, T., Schwarz, D., Fischer, M., et al. (2016). Correlated magnetic resonance imaging and ultramicroscopy (MR-UM) is a tool kit to assess the dynamics of glioma angiogenesis. Elife *5*, e11712. https://doi.org/10.7554/eLife.11712.
42. Lanitis, E., Irving, M., and Coukos, G. (2015). Targeting the tumor vasculature to enhance T cell activity. Curr. Opin. Immunol. *33*, 55–63. https://doi.org/10.1016/j.coi.2015.01.011.
43. Lamplugh, Z., and Fan, Y. (2021). Vascular Microenvironment, Tumor Immunity and Immunotherapy. Front. Immunol. *12*, 811485. https://doi.org/10.3389/fimmu.2021.811485.
44. Teillaud, J.L., Houel, A., Panouillot, M., Riffard, C., and Dieu-Nosjean, M.C. (2024). Tertiary lymphoid structures in anticancer immunity. Nat. Rev. Cancer *24*, 629–646. https://doi.org/10.1038/s41568-024-00728-0.
45. Guelfi, S., Hodivala-Dilke, K., and Bergers, G. (2024). Targeting the tumour vasculature: from vessel destruction to promotion. Nat. Rev. Cancer *24*, 655–675. https://doi.org/10.1038/s41568-024-00736-0.
46. Meng, X., Wu, T., Hong, Y., Fan, Q., Ren, Z., Guo, Y., Yang, X., Shi, P., Yang, J., Yin, X., et al. (2022). Camrelizumab plus apatinib as second-line treatment for advanced oesophageal squamous cell carcinoma (CAP 02): a single-arm, open-label, phase 2 trial. Lancet. Gastroenterol. Hepatol. *7*, 245–253. https://doi.org/10.1016/s2468-1253(21)00378-2.
47. Dinh, H.Q., Pan, F., Wang, G., Huang, Q.F., Olingy, C.E., Wu, Z.Y., Wang, S.H., Xu, X., Xu, X.E., He, J.Z., et al. (2021). Integrated single-cell transcriptome analysis reveals heterogeneity of esophageal squamous cell carcinoma microenvironment. Nat. Commun. *12*, 7335. https://doi.org/10.1038/s41467-021-27599-5.
48. Murray, E., Cho, J.H., Goodwin, D., Ku, T., Swaney, J., Kim, S.Y., Choi, H., Park, Y.G., Park, J.Y., Hubbert, A., et al. (2015). Simple, Scalable Proteomic Imaging for High-Dimensional Profiling of Intact Systems. Cell *163*, 1500–1514. https://doi.org/10.1016/j.cell.2015.11.025.
49. Lee, E., Choi, J., Jo, Y., Kim, J.Y., Jang, Y.J., Lee, H.M., Kim, S.Y., Lee, H.J., Cho, K., Jung, N., et al. (2016). ACT-PRESTO: Rapid and consistent tissue clearing and labeling method for 3-dimensional (3D) imaging. Sci. Rep. *6*, 18631. https://doi.org/10.1038/srep18631.
50. Yip, R.K.H., Rimes, J.S., Capaldo, B.D., Vaillant, F., Mouchemore, K.A., Pal, B., Chen, Y., Surgenor, E., Murphy, A.J., Anderson, R.L., et al. (2021). Mammary tumour cells remodel the bone marrow vascular microenvironment to support metastasis. Nat. Commun. *12*, 6920. https://doi.org/10.1038/s41467-021-26556-6.

STAR★METHODS

KEY RESOURCES TABLE

REAGENT or RESOURCE	SOURCE	IDENTIFIER
Antibodies		
rat anti-mouse CD31, Clone MEC 13.3 (RUO)	BD Biosciences	Cat# 550274; RRID:AB_39357
rabbit anti-CD3ε (E4T1B)	Cell Signaling Technology	Cat# 78588; RRID:AB_2889902
rabbit anti-CD4 [EPR19514]	Abcam	Cat# ab183685; RRID:AB_2686917
donkey anti-rabbit IgG, Alexa Fluor 647	Thermo Fisher Scientific	Cat# A-31573; RRID:AB_2536183
donkey anti-rat IgG, Alexa Fluor 555	Abcam	Cat# ab150154; RRID:AB_2813834
Chemicals, peptides, and recombinant proteins		
4-Nitroquinoline N-oxide (4NQO)	Sigma–Aldrich	Cat# N8141
3-[(3-Cholamidopropyl)dimethylammonio]-1-propanesulfonate (CHAPS)	BBI	Cat# A600110-0005
heptakis(2,6-di-*O*-methyl)-β-cyclodextrin	Leyan	Cat# 51166-71-3
dichloromethane (DCM)	Sigma-Aldrich	Cat# 270997
benzyl ether (DBE)	Sigma-Aldrich	Cat# 108014
Critical commercial assays		
FDISCO Kit	JARVIS	JA11011
CUBIC-L	TCI	T3740
CUBIC-R+(M)	TCI	T3741
Deposited data		
Image analysis data	This paper	https://doi.org/10.17632/rggyy48rg6.1
Experimental models: Organisms/strains		
Mouse: C57BL/6	The Jackson Laboratory	RRID:MGI:7264769
Software and algorithms		
Imaris 10.0.0	Oxford Instruments	N/A
FIJI (ImageJ)	Hawkins, E. D. et al.[25]	N/A
GraphPad Prism 8	GraphPad	N/A
Other		
confocal dish	Biosharp	BS-20-GJM-20

EXPERIMENTAL MODEL AND STUDY PARTICIPANT DETAILS

Mice

Animal experiments were performed according to the guidelines provided by Shenzhen PKU-HKUST Medical Center Animal Ethics Committee (No. 2022-1223). Six-week-old female C57BL/6 mice were purchased from Topbiotech Company and housed in a special pathogen-free environment under controlled conditions (20°C–22°C, 12-h light/dark cycle, *ad libitum* food). To induce multistage ESCC, mice were exposed to 4NQO (Sigma–Aldrich, N8141) for 16 weeks at a concentration of 100 μg/mL in drinking water, followed by replacement with sterile water until euthanasia. Drinking water was refreshed weekly.

METHOD DETAILS

Sample collection and preparation

Esophagi of 4NQO-induced mice were dissected at five time points: week 0, 6, 13, 17, 25 after treatment. Mice were anesthetized, perfused with heparinized PBS (10 U/mL heparin concentration, BBI, A603251-0001; PBS pH 7.4, Gibco, C10010500BT) and subsequently with 4% PFA (Solarbio, P1110). The perfusion rate was maintained below 10 mL/min for 6–10 min. Esophagi were then cut vertically and postfixed for 15 h at 4 °C (Figure S1A).

Antibody validation

Frozen sections (20 μm) of PFA-fixed tissue were used to assess the methanol compatibility of the antibodies.[20] Sections were initially incubated in 100% methanol for 3 h, while non-methanol treatment was used as a positive control. To enhance antibody penetration in thick sections, extended incubation time was conducted. Specifically, frozen sections were blocked with 5% donkey serum (Jackson ImmunoResearch Laboratories, 017-000-121) and 2% BSA (Beyotime, ST025) for 1 h. Next, incubation with primary antibodies in 2.5% donkey serum and 1% BSA for 20 h at 4 °C. After washing, incubation with secondary antibodies in PBS for 1.5 h, followed by DAPI for nuclear visualization. The sections were imaged using a confocal microscopy. If the signal-to-noise was diminished after methanol pretreatment, iDISCO sample pretreatment without methanol would be used.

Whole-tissue immunolabeling

The Passive-wildDISCO protocol is primarily derived from wildDISCO.[32] Instead of using a pump for whole-body perfusion, passive incubation with wildDISCO immunostaining buffers is effective and economical for esophagus.

The iDISCO-Prolonged incubation protocol followed the detailed iDISCO+ procedures.[20] The differences lie in the extended antibody incubation time and washing time, which were prolonged to 7–10 days and 2–2.5 days, respectively.

The iDISCO-Centrifugation protocol combined iDISCO+ methods with c-PRESTO steps.[49] In brief, the iDISCO+ antibody incubation solution was centrifuged at 500 × g for 4 h every day. During 4 days of incubation, primary antibody concentration increased daily. Notably, the tissue could be curved after centrifugation, which can be revised by the holder (Figure S1D) in subsequent light-sheet fluorescence microscopy. Additionally, the washing time was extended to 2–2.5 days.

Three immunolabeling protocols are described below in detail. All solutions must be filtered using a filter and supplemented with 0.02% NaN_3.

Passive-wildDISCO protocol

The fixed esophagus was washed with PBS for 1h three times and then incubated for 1.5 days with 5 mL of PBS/2% Triton X-100/10% Donkey serum. Next, incubation with primary antibodies for 7 days in 1.8 mL of immunostaining buffer (3% Donkey serum, 2% Triton X-100, 10% CHAPS (BBI, A600110-0005), 1% Glycine, 10% DMSO, and 1% Heptakis(2,6-di-*O*-methyl)-β-cyclodextrin (Leyan, 51166-71-3) in PBS). Primary antibodies: CD3 (CST, 78588, 1:400), CD31 (BD, 550274, 1:20). The tissue was washed 8 times with 15 mL PBS for 2 days. Next, the tissue was incubated with secondary antibodies (Thermo Fisher Scientific, 1:1000) and DAPI (Sigma, D9542, 1:500) in the same immunostaining buffer. The tissue was then washed 10 times with PBS for 2 days. All steps were performed on a rotator at room temperature.

iDISCO-prolonged incubation protocol

The fixed esophagus was washed and then incubated with 5 mL of PBS/0.2% Triton X-100 (PTx.2) for 1 h twice, RT. The tissue was incubated overnight with 5 mL of PTx.2/20%DMSO and then incubated overnight with 5 mL of PBS/0.1% Triton X-100/0.1% Tween 20/0.1% Deoxycholate/0.1% NP40/20% DMSO at 37°C. Next, the tissue was washed in 5 mL PTx.2 for 1 h twice, RT. After pretreatment, the tissue was penetrated in 5 mL 0.2% Triton X-100/0.3M Glycine/20% DMSO and blocked in 6% Donkey serum/0.2% Triton X-100/10% DMSO for 2 days on a rotator at 37°C, respectively. Next, the tissue was incubated with primary antibodies in 1.8 mL 0.2% Tween 20/10 μg/mL Heparin/5% DMSO/3% Donkey serum for 7–10 days at 37°C. The tissue was washed in 15 mL PBS/0.2% Tween 20/10 μg/mL Heparin (PTwH) 8 times for 2 days, RT. Next, the tissue was incubated with secondary antibodies and DAPI in 1.8 mL PTwH/3% Donkey serum for 7–10 days, 37°C. The tissue was then washed in 15 mL PTwH 10 times for 2.5 days, RT.

iDISCO-centrifugation protocol

The tissue was pretreated, permeabilized, and blocked using the same method as described in the iDISCO-Prolonged incubation protocol. Next, incubation with primary antibodies for 4 days with centrifugation at 500 × g for 4 h every day. During 4 days of incubation, primary antibody concentration increased daily (1:1000, 800, 600, 400; 1:80, 60, 40, 20). The tissue was washed with PTwH 8 times for 2 days, RT. Next, the tissue was incubated with secondary antibodies and DAPI with centrifugation mentioned above. Finally, the tissue was washed with PTwH 10 times for 2.5 days, RT.

Esophageal clearing

Esophageal clearing in this pipeline used the iDISCO+ clearing method. After immunolabeling, the tissue was transferred to a 5 mL snap cap vial (VWR, VWRI548-0554) wrapped in tinfoil. The tissue was dehydrated with 5 mL of methanol/H_2O solution (20%, 40%, 60%, 80%, 100%, 1 h each) and then incubated overnight in 100% methanol. Next, incubation with 66% DCM (Sigma-Aldrich, 270997)/33% methanol for 3 h. The tissue was then incubated in 100% DCM for 15 min twice. These steps were performed on a rotator (rpm<25). Finally, the tissue was preserved in DBE (Sigma-Aldrich, 108014). All steps must be conducted within a fume hood.

The FDISCO and CUBIC methods were performed according to the FDISCO Kit (JARVIS, JA11011) and CUBIC-L/R+(M) (TCI, T3740/T3741), respectively.

Light-sheet microscopy

Whole-tissue (approximately 8 × 2 × 0.7–1.3 mm^3) was imaged using a light-sheet fluorescence microscopy (LSFM) (Litone, XL) at 2048 × 2048 pixels with a custom 10× objective (Olympus, XLPLN10XSVMP/NA 0.6/maximum working distance, 7.2 mm), which clearly visualized T cells. Multichannel images were acquired using the following fluorescent labels: DAPI, Alexa Fluor 555, and Alexa Fluor 647, with a voxel size of 0.58 × 0.58 × 2 μm. All images were stitched to intact 3D images using the Litscan plugin.

Histological categories

After 3D imaging, the tissues were de-cleared in 100%, 100%, 80%, 60%, 40%, 20% methanol/H_2O solutions for 1 h each and in PBS overnight on a rotator. The tissues were then placed in a series of alcohol/H_2O solutions (75%, 85%, 90%, 95% for 40 min and 100% ethanol for 30 min twice). Next, immersion with xylene for 30 min twice before being embedded in paraffin. These steps followed the DIPCO method.[33]

The paraffin-embedded tissues were consecutively sectioned for hematoxylin–eosin (H&E) examination. Histological categories were determined based on defined criteria.[4] In our study, the NOR stage (Normal) corresponded to 0 weeks after 4NQO treatment and showed a well-organized stratified epithelium. Stage INF (Inflammation) corresponded to 13 weeks after treatment and showed that the mucosa was infiltrated by lymphocytes. The PINF (Pre-inflammation) stage was defined as half of INF phase and corresponded to 6 weeks after treatment. PINF closely resembled NOR pathologically, but the mucosal microenvironment had already changed. Stage DYS (Dysplasia) corresponded to 17 weeks after treatment and was defined as atypical cells in the epithelium but not full thickness. Stage ICA (Invasive carcinoma) corresponded to 25 weeks after treatment and was defined by the invasion of atypical cells into subepithelial tissues.

Image processing and analysis

3D image processing and analyses were mainly performed using Imaris (v.10.0.0). Three mucosal or tumor regions of three esophagi per stage were randomly selected for the analyses, with a per cubic volume from approximately 700 × 250 × 40 μm^3 to 600 × 300 × 60 μm^3, considering the variable position of the esophageal mucosa in each XY plane. For blood vessel segmentation, CD31-positive signals were detected by the AI-powered filament tracer, which included the automated autopath algorithm and manual creation. $CD3^+$ T cells were rendered using spots with the diameter of 8 μm and default quality filter. T cell aggregates were identified using the surface function setting a minimum (20 μm) and maximum (200 μm) diameter and counted within the ROI of 6 × 1.2 × 0.4 mm^3 per esophagus. Vascular analysis in regions with or without T cell aggerates was conducted on three regions from three mice per stage, with a per cubic volume of 600 × 300 × 60 μm^3. The tumor surface was determined by a manual tracing wizard, and the distribution of T cells at different distances from the tumor margin could be found as the location with the shortest distance to the surface in the statistical module.

To evaluate the spatial distance between vessels and T cells, 3D random spots were generated. In brief, a cubic ROI image in Imaris was imported to Fiji, and a published Fiji macro was carried out to create random spots.[25,50] Notably, the random size was calculated as the spot diameter divided by pixels. The random spot images were then exported by Fiji bio-formats plugin. Next, all images were converted to ims format by ImarisFileConverter. The image was finally added to the Imaris channel, and the distance between vessels and T cells could be computed using the shortest distance statistical value.

Quantification of the mean fluorescence intensity at various imaging depths was conducted using Fiji. The mean fluorescence intensity was then normalized to that of the superficial slide using Excel.

QUANTIFICATION AND STATISTICAL ANALYSIS

Statistical analyses were conducted using GraphPad Prism 8. Shapiro-Wilk test was conducted to evaluate the normality ($n < 50$). The significance between two groups was determined using two-tailed unpaired t tests (normal distribution/$n > 50$) or Mann-Whitney U tests (nonnormal distribution). All data were presented as mean ± s.e.m. $p < 0.05$ was considered as statistical significance.